Journal of Environmental Chemical Engineering 5 (2017) 4365–4373

Contents lists available at ScienceDirect

Journal of Environmental Chemical Engineering

journal homepage: www.elsevier.com/locate/jece

Research paper

Photocatalytic degradation using one-dimensional TiO_2 and Ag-TiO_2 nanobelts under UV-LED controlled periodic illumination

Robert Liang[a,b,*], Lena C.M. Li Chun Fong[a,c], Maricor J. Arlos[c], Jocelyn Van Leeuwen[a], Emad Shahnam[a], Peng Peng[d], Mark R. Servos[c], Y. Norman Zhou[a,b]

[a] Centre for Advanced Materials Joining, Department of Mechanical and Mechatronics Engineering, University of Waterloo, Waterloo, Ontario, N2L 3G1, Canada
[b] Waterloo Institute of Nanotechnology, University of Waterloo, Waterloo, Ontario, N2L3G1, Canada
[c] Department of Biology, University of Waterloo, Waterloo, ON, Canada
[d] School of Mechanical Engineering and Automation, International Research Institute for Multidisciplinary Science, Beihang University, 37 Xueyuan Rd, Beijing, 100191, China

ARTICLE INFO

Keywords:
Controlled periodic illumination
Silver
Titanium dioxide
Nanobelts
UV-LED
Photocatalysis
Environmental remediation
Advanced oxidation processes

ABSTRACT

Semiconductor photocatalysis such as ultraviolet/TiO_2 (UV/TiO_2) can be used in environmental remediation. It is an advanced oxidation process that can degrade organic contaminants through redox reactions. Unmodified TiO_2 can only generate electron-hole pairs in the UV range so it has limited efficiency. Highly efficient materials are required for this process to be implemented at a large scale. In this study, three methods were used to investigate and improve the efficiency of UV/TiO_2 slurry systems: (i) synthesizing one-dimensional TiO_2, (ii) formation of Schottky junctions, and (iii) application of UV-light emitting diode (UV-LED) under controlled periodic illumination (CPI). These methods were quantified by measuring the formation of 2-hydroxyterephthalic acid (HTPA) as a probe molecule. In order to improve the charge separation in TiO_2, one-dimensional TiO_2 nanobelts (TNB) were synthesized using a hydrothermal method and Ag nanoparticles were deposited on these nanobelts to form metal-semiconductor junctions. Ag-TNB was found to have HTPA formation rate greater than 1.33 and 2.59 times than that of P25 and TNB, respectively, under continuous illumination. UV-LED CPI was used to explore changes in photonic efficiencies by using duty cycles from 10% to 100%. At a duty cycle of 10%, normalized HTPA formation rate was 1.75, 1.40, and 0.70 times the HTPA formation rate at continuous illumination for commercial TiO_2 (P25), TNB, and Ag-TNB nanomaterials, respectively. The pulse frequency was varied from 0.05 Hz to 25 Hz. Under high frequencies, the HTPA formation rate was greater for Ag-TNB and P25 samples compared to the lowest frequency (0.05 Hz). Ag-TNB was determined to be an effective photocatalyst using CPI by demonstrating photon-limiting behaviour when lowering the duty cycle.

1. Introduction

Photocatalysis has applications in environmental remediation such as air pollution control and water treatment. Titanium dioxide (TiO_2) is the most commonly used and studied material due to its biocompatibility, non-toxicity, and commercial availability [1]. However, electron-hole pairs can only be generated under UV radiation, which limits the use of conventional TiO_2 in advanced oxidation processes (AOP) in water treatment. Additionally, recombination losses are inherent in semiconductors, further reducing the overall efficiency [2].

There have been attempts to increase both the photonic efficiency and visible light absorption by optimizing material properties and/or physical operational parameters. The photonic efficiency may be improved by changing the material properties of TiO_2. For instance, decreasing the bandgap energy of TiO_2 via metal [3,4] and non-metal doping [5–8] allows TiO_2 to generate electron-hole pairs under visible light. The incoming radiation may be maximized by both slow photons and stop-band reflection using SnO_2-TiO_2 composites [9]. Other studies have attempted to reduce recombination losses by creating metal-semiconductor (Schottky) junctions [10–13] and synthesizing one-dimensional (1-D) TiO_2 nanomaterials (nanowires, nanorods, and nanotubes) that have greater electron transport than nanoparticles [14–17].

Photonic efficiency can also be improved by optimizing the operational parameters of TiO_2 photocatalytic processes such as catalyst concentration, light intensity, pH, temperature, and addition of oxidant [18]. Temperature control and the addition of pH-adjusting chemicals

* Corresponding author at: Department of Mechanical and Mechatronics Engineering, University of Waterloo, Waterloo, ON, Canada, N2L 3G1, Canada.
E-mail addresses: rliang@uwaterloo.ca, rliang66@gmail.com (R. Liang).

http://dx.doi.org/10.1016/j.jece.2017.08.019
Received 7 June 2017; Received in revised form 5 August 2017; Accepted 15 August 2017
Available online 20 August 2017

increase operational costs. AOPs combining TiO_2 photocatalysis with chemical oxidants, such as hydrogen peroxide and ozone, can increase efficiency, but this also comes at an additional cost [19–23].

The photocatalytic reaction order is dependent on the irradiance and an increase in the light irradiance results in lower photonic efficiency [18]. There are three light irradiance regimes: (i) low, (ii) intermediate, and (iii) high irradiance. At the low irradiance regime, the reaction rate is linearly proportional to the irradiance. At intermediate intensity, the reaction rate varies by the square root of the irradiance. At high intensity, the reaction rate is independent of the irradiance [24]. Under the latter two irradiance regimes, photocatalysis suffers in efficiencys. Because of these limitations, UV-LEDs are more favourable compared to mercury lamps, especially under low pollutant concentrations [25].

Most photocatalytic studies until recently were conducted using low and medium pressure mercury lamps as UV light sources [26,27]. However, these suffer from warm-up time, reliability, durability, and efficiency [28,29]. Other studies have focused on using solar radiation in TiO_2 applications [30,31] but are only feasible in locations where solar radiation is abundant. LEDs are more efficient because the quantum yields are close to unity and also have higher lifetimes than mercury lamps [32]. Furthermore, mercury lamps cannot be alternatively turned on and off effectively on the millisecond time-scale. Based on previous studies, LEDs under controlled periodic illumination (CPI) were more effective for photocatalysis using xenon lamp illumination and a mechanical shuttering system [29,33].

One way to reduce recombination is to introduce noble metals such as gold [34], platinum [3,35], palladium [36], and silver [37,38] that serve as electron sinks for photogenerated electrons. Recombination is controlled by the formation of a Schottky barrier between surface metal particles and semiconductor photocatalyst[39]. Besides the reduction of recombination, the use of silver is beneficial due to being: (i) a relatively inexpensive noble metal, (ii) an effective and known disinfectant [40], and (iii) a thermal catalyst under localized surface plasmon resonance (LSPR) conditions that prevent deactivation of photocatalysts [41].

The objective of this study was to explore the effect of CPI on the photonic efficiency of UV-LED irradiation TiO_2 process in a batch slurry reactor by using the temporal decomposition of terephthalic acid (TPA) as a probe and several TiO_2-based nanomaterials. This is the first study to investigate CPI effects on one-dimensional TiO_2 nanobelt (TNB) and silver nanoparticle − TNB (Ag-TNB) composite nanomaterials. The decomposition of malachite green (MG) was also assessed under continuous illumination. In this study, three procedures were used to decrease recombination processes: (i) conversion of nanoparticles into a 1-D TNB, (ii) addition of Ag nanoparticles onto TiO_2, and (iii) the utilization UV-LED controlled CPI processes. The effects of UV-LEDs under various duty cycles were explored. TNB and Ag-TNB were compared to commercial P25 nanoparticles under CPI to increase kinetic rates by preventing charge carrier recombination.

2. Experimental

2.1. Reagents and chemicals

Titanium Dioxide (P25 Aeroxide™), silver nitrate ($AgNO_3$), hexamethylenetetramine (HMTA), hydrochloric acid (HCl), and sodium hydroxide (NaOH) were used in TiO_2 synthesis procedures. Terephthalic acid (TPA) and malachite green (MG) were used as model pollutant compounds for photocatalytic experiments. All materials were purchased from Sigma-Aldrich. Ultrapure water was obtained from a MilliQ water purification system which was operated at 18.2 MΩ cm resistivity and < 5 μg/L total organic carbon (TOC) at 25 °C (EMD Millipore).

2.2. TiO_2 synthesis methods

2.2.1. TiO_2 nanobelt synthesis

TiO_2 nanobelts were synthesized using a modified method developed previously [42]. In a 125 mL stainless steel acid digester with a insertable Teflon cup (Parr Instruments), P25 Aeroxide™ (2 g) was added into the Teflon cup containing a solution of NaOH (60 mL, 10 M). The cup was inserted into the stainless steel body, sealed, and placed in a muffle furnace at 250 °C with a ramp rate of 10 °C min^{-1}. After 24 h at the setpoint, the furnace was turned off and cooled naturally. The sodium titanate ($Na_2Ti_3O_7$) nanobelts settled at the bottom and the excess alkaline solution was decanted and discarded. The $Na_2Ti_3O_7$ was transferred into a beaker and ultrapure water (400 mL) was added to disperse the solution. The solution was then transferred into eight 50 mL conical tubes and centrifuged four times at 3500 rpm for 10 min each. Subsequently, the nanobelts were transferred into a beaker containing a solution of HCl (400 mL, 0.1 M), and through an ion exchange process hydrogen titanate ($H_2Ti_3O_7$) was obtained. Excess chloride ions were removed by washing with ultrapure water, centrifuging samples, and decanting the supernatant. This process was repeated three times. Afterward, $H_2Ti_3O_7$ was dried in a furnace for 80 °C for 8 h and subsequently heat treated at 700 °C for 2 h to form TNB. The maximum yield was around 90% from the synthesis step.

2.2.2. Ag-TiO_2 nanobelt synthesis

$H_2Ti_3O_7$ nanobelts from the TNB synthesis were used in the preparation of Ag-TNB. In a solution containing a solution of H_2SO_4 (60 mL, 0.02 M), the precursor (1 g) was added in the acid digester and kept at 100 °C for 12 h. The products were centrifuged, washed with ultrapure water several times, and dried at 70 °C overnight. The hydrogen titanate, $H_2Ti_3O_7$, obtained by acid treatment was heated at 700 °C for 2 h to form TNB. A hydrothermal method was used to create nano-heterostructures of Ag nanoparticles on TNB [38]. Treated TNB (1 g) was added to a 125 mL acid digested containing 60 mL of $AgNO_3$ (1 mM) and HMTA (2 mM). The acid digester was heat treated for 4 h at 100 °C. Ag ions in solution were removed by washing with ultrapure water, centrifuging samples, and decanting the supernatant. This process was repeated three times. The Ag-TNB was dried in the furnace at 80 °C for 8 h.

2.3. Nanomaterial characterization

The surface morphology of TiO_2 nanomaterials was characterized using field emission scanning electron microscopy (FE-SEM, Zeiss LEO 1550), while the specific surface area was determined using a Bruauner-Emmett-Teller (BET) surface analyzer (Quantachrome Autosorb iQ) using nitrogen gas adsorption data. The bandgap of TiO_2 samples were determined by recording the diffuse reflectance spectra (DRS) using a Shimadzu UV-2501PC UV–vis-NIR spectrophotometer with an integrating sphere. A Raman spectrometer (Renishaw Ramanscope) equipped with a He-Ne laser (5 mW incident power, 633 nm wavelength) was used to obtain spectra associated with different TiO_2 crystalline phases. X-ray diffraction (XRD) was determined using an Inel powder X-ray Diffractometer XRD) with Cu-Kα_1 radiation and a position sensitive detector. X-ray photoelectron spectroscopy (XPS) was carried out to verify the presence of TiO_2 and Ag. The measurement was conducted using a VG Scientific ESCALab 250 system, using an aluminum Kα radiation source ($h\nu$ = 1486.6 eV) under ultra-high vacuum. A survey scan was collected at 50 eV pass energy, whereas individual scans were collected at 20 eV pass energy. Ti 2p (Fig. S3b), O 1 s (Fig. S3c), and Ag 3d (Fig. S3d) regional spectra were obtained and their peaks were deconvoluted.

The isoelectric point (IEP) of engineered nanomaterials was obtained measuring the zeta potential of the nanomaterial at pH values ranging from 3 to 10. Zeta potential measurements were conducted with 0.1 g L^{-1} in ultrapure water and adjusted to various pH values

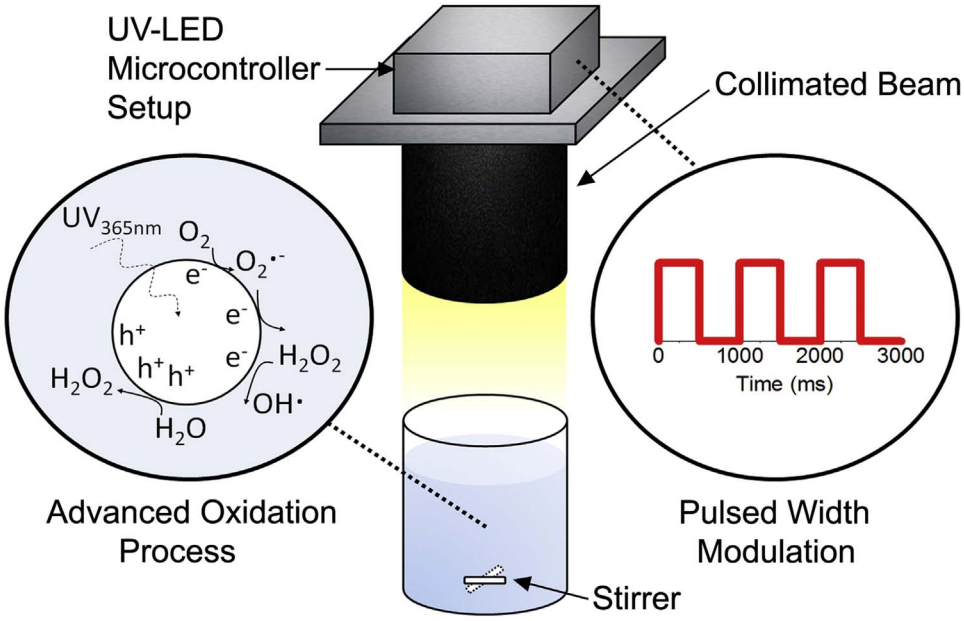

Fig. 1. Schematic of UV-LED/TiO_2 advanced oxidation under pulsed width modulation.

using NaOH or HCl. No salt, such as NaCl, was added as is the case with methods used by others to measure zeta potential in order to simulate experimental conditions [43]. The zeta potential analyzer was programmed to six measurements for each sample.

2.4. Standardization and setup

A schematic of the UV-LED/TiO_2 process under pulsed-width modulation (PWM) is shown in Fig. 1. The setup consisted of multi-position stir plate and collimated UV-LED setup as mentioned in Arlos et al. [44] The UV-LED was controlled using a microcontroller (Arduino) coupled with a LED Current Driver (LEDSEEDUINO) and PWM script (See Section S1 in the Supporting Information Document) was programmed into the controller. The average power output of the UV-LED lamps was measured using a Thorlabs power and energy meter (PM100-USB). The light pulse frequency of LEDs was controlled with various illumination and dark periods listed in Table 1. The pulse frequency and duty cycle was calculated as:

$$\textit{Pulse frequency}, \nu = \frac{1}{t_{on} + t_{off}} \quad (1)$$

$$\textit{Duty cycle}, \gamma = \frac{t_{on}}{t_{on} + t_{off}} \quad (2)$$

Table 1
Light profiles for continuous and periodic illumination showing duty cycle and frequency of pulsing.

Duty Cycle (γ)	Average UV intensity ($m\,W\,cm^{-2}$)	t_{on} (ms)	t_{off} (ms)	Period (ms)
Duty cycle experiments at constant frequency				
10%	0.22	100	900	1000 (1 Hz)
25%	0.54	250	750	
50%	1.08	500	500	
75%	1.63	750	250	
100%	2.18	Continuous illumination		
Frequency experiments at constant duty cycle				
50%	1.08	10000	10000	20000 (0.05 Hz)
50%	1.08	1000	1000	2000 (0.5 Hz)
50%	1.08	100	100	200 (5 Hz)
50%	1.08	20	20	40 (25 Hz)

where t_{on} and t_{off} were the length of time that the UV-LED was on and off, respectively.

2.5. Photocatalytic degradation

2.5.1. Malachite green degradation and pseudo first-order kinetic model

A 60 ppm malachite green (MG) stock solution was prepared by dissolving MG (60 mg) in ultrapure water (1 L). Three replicates of MG solution (300, 10 ppm) were made by mixing 60 ppm MG stock (50 mL) and ultrapure water (250 mL). The tested TiO_2 nanomaterials were P25, TNB, and Ag-TNB. In each test, TiO_2 nanomaterials were added to each replicate for a final concentration of 0.1 g L^{-1}. The beakers were placed in the multi-position stir plate and the solutions were stirred at 600 rpm for the duration of the experiment.

Prior to UV exposure, a 60 min equilibration period was set under dark conditions for the adsorption of MG onto TiO_2 nanomaterials. Aliquots were sampled throughout the 300 min time span of the experiment. The samples were centrifuged at 5000 rpm for 5 min to remove TiO_2 nanomaterials from solution. The supernatant was then transferred to a 96 well-plate for MG degradation analysis. The endpoint adsorption of MG was measured at a wavelength of 615 nm against a calibration curve.

The photocatalytic degradation of MG was evaluated using Langmuir-Hinshelwood kinetics [45]. The model assumed low concentrations of MG (C < < mM,). Therefore, the analysis was simplified using a pseudo-first order equation:

$$\frac{dC}{dt} = -k_{app} C \quad (3)$$

and can be rearranged to its integrated form:

$$\ln\left(\frac{C}{C_o}\right) = -k_{app} t \quad (4)$$

where k_{app} (min^{-1}) is the apparent first-order reaction rate constant. A linear plot of $ln(C/C_0)$ vs. t was plotted and a linear regression was conducted to obtain the apparent kinetic rate, k_{app}.

2.5.2. TPA degradation and HTPA formation kinetic model

A similar TPA degradation and HTPA fluorescence method was used from work conducted previously [44]. In a beaker, TPA (0.831 g) was dissolved in NaOH (300 mL, 6 mM). TiO_2 nanomaterials were added to the solution for a final TiO_2 concentration of 0.1 g L^{-1}. The

experiments were conducted under illumination for 240 min and aliquots (1 mL) were taken at several time points.

TPA undergoes a reaction with a hydroxyl radical, producing 2-hydroxyterephthalic acid (HTPA) [44,46]. The HTPA concentration was monitored using a fluorescence plate reader (SpectraMax M3, Molecular Devices). Under excitation mode (λ_{ex} = 315 nm), an emission spectra from 350 to 550 nm was used. A HTPA standard curve was included in the plate to quantify the amount of HTPA formed during TPA degradation. The standard curve was generated from the intensity of the peak emission wavelength of each spectrum.

The formation constant rate, k_1, of HTPA, which is the first degradation product of TPA, was studied. In the first minutes of the experiment, there is an excess of TPA and the concentration of HTPA rapidly increases (first reaction step − formation of HTPA) due to the oxidation of TPA by holes and/or hydroxyl radicals formed on the surface of the TiO_2 nanomaterial. As the HTPA concentration increased over time, its degradation rate also increases (second reaction step). An equilibrium concentration is reached, in which the rates of formation and degradation of HTPA are equal. A simplified kinetic model for HTPA was proposed by Černigoj et al. [46]:

$$\frac{dC_{HTPA}}{dt} = k_1 - k_2 C_{HTPA} \tag{5}$$

where C_{HTPA} represents the molar concentration of HTPA, k_1 represents the zero-order HTPA formation rate, and k_2 represents the pseudo-first order kinetic degradation rate. The fitting function was represented by the equation [46]:

$$C_{HTPA} = \frac{k_1}{k_2}\left(1 - e^{-k_2 t}\right) \tag{6}$$

In order to compare the photocatalysts used in the study, only the initial rate constant k_1 (first reaction step) was considered.

3. Results and discussion

3.1. Materials characterization

Three types of TiO_2 nanomaterials were investigated: P25, TNB, Ag-TNB and their material characteristics are presented in Table 2 (See Fig. S1 for the (a) Tauc plot, (b) Raman spectra, and (c) zeta potential and Fig. S2 for the XRD measurements). The SEM images of the nanomaterials are shown in Fig. 2. P25 contains clustered particles that range from 10 to 30 nm, which is in the range reported from the manufacturer (21 nm). TNB images show nanobelts that range from 20 to 100 nm in width and μm lengths. This size distribution is consistent with previous studies [42,47]. The TNB samples are also composed of nanoparticles and truncated rods fused on the surface of the nanobelt. Ag-TNB images are similar in morphology to TNB samples and show no obvious Ag nanoparticles on the TNB using both Raman spectroscopy (Fig. S1b) and XRD (Fig. S2), however, a purple tinge can be observed visually in Fig. S1d. XPS analysis was conducted in order to verify that Ag was deposited on TNB. XPS analysis (Fig. S3) revealed the presence Ag^0 peaks at 368.4 eV and 374.4 eV, which corresponds to the Ag $3d_{5/2}$ and Ag $3d_{3/2}$ peaks. Because of the growth along one dimension and larger structure than P25, the synthesized 1-D TiO_2 nanomaterials settled faster in aqueous solution. The zeta potential can describe the stability of the dispersion and the average values obtained for P25, TNB, and Ag-TNB were −12.15 mV, −6.45 mV, and −8.60 mV, respectively, at the experimental pH of 11 used in this study. P25 is more stable than the synthesized nanomaterials in solution, however all the nanomaterials will settle over time under a zeta potential magnitude of less than 30 mV under no external agitation.

Table 2
Material Characterization of TiO_2 nanomaterials.

Material Measurement	P25	TNB	Ag-TNB
BET Surface Area ($m^2\,g^{-1}$)	57	20	87
DFT Pore Volume Method ($cm^3\,g^{-1}$)	0.12	0.03	0.24
Zeta potential at TPA experimental pH (mV)	−12.15	−6.45	−8.6
Bandgap energy (eV)	3.02	2.95	3.20
Crystal phase	Anatase/Rutile Mixture	Anatase	Anatase/Rutile Mixture

All three nanomaterials contain anatase as the predominant crystalline phase as confirmed through Raman spectroscopy with characteristic peaks as referenced through the RRUFF online database (R060277 and R050417) and XRD. This is also confirmed through diffuse reflectance spectroscopy in which the bandgap energy is between 2.95–3.20 eV, characteristic for TiO_2 anatase and indicates that only radiation below 400 nm is capable of generating electron-hole pairs in all samples.

The surface area can impact adsorption capacity and photocatalytic activity, though the latter does not a correlate linearly to surface area; it depends on the other factors such as the contents of the water matrix used. The BET surface area of P25, TNB, and Ag-TNB were 57, 20, and 87 $m^2\,g^{-1}$, respectively. TNB has a lower surface area due to fusing of P25 nanoparticles during the hydrothermal process, reducing the overall surface area compared to P25. Ag-TNB has a higher surface area due to the acid corrosion step preceding Ag deposition that increases porosity.

3.2. Photocatalytic performance under continuous illumination

HTPA formation rate from TPA degradation and MG apparent removal rate coefficients were determined using P25, TNB, and Ag-TNB (Fig. 3). MG was used as a model dye pollutant to compare various catalysts. Its advantage is that it is not susceptible to dye decolourization under UVA radiation compared to visible light irradiation [25]. There was no statistical difference between the absolute kinetic rate coefficients of P25 and TNB, however there was a difference with Ag-TNB ($p < 0.017$) for both MG removal and HTPA formation rates (Table S2A for one-way ANOVA test). Even though the P25 and TNB have similar TPA formation rates, the recombination rate of 1-D TiO_2 is generally lower when compared to nanoparticles due to a decrease of grain boundary defects when joining nanoparticles into a 1-D structure, which decreases charge transfer resistance [48,49].

3.2.1. Electron lifetime of TiO_2 nanoparticles compared to nanobelts

To test that nanobelts have a lower recombination rate than nanoparticles, the electron lifetime of the nanomaterials were compared. P25 nanoparticles and TNB were cast on fluorine-tin oxide (FTO) glass using an electrodeposition method and tested using a photoelectrochemical setup (See Section S2 and S3 in the Supporting Information). Under open circuit conditions, the photogenerated electrons accumulate within TiO_2 photoanode and react with its aqueous environment. At steady state conditions, the rate of electron accumulation reaches equilibrium with the rate of electron loss [50,51]. The electron lifetime of the photoelectrode can be found from the change in open circuit potential, V_{OC}, upon termination of UV illumination. Electron recombination kinetics at the semiconductor interface can be analyzed from the decay rate. The decay rate, τ, can be calculated via the following equation [50–52]:

$$\tau = -\left(\frac{k_B T}{e}\right)\left(\frac{dV_{OC}}{dt}\right)^{-1} \tag{7}$$

where k_B is Boltzmann constant, T is the temperature, and e is the elementary charge.

The TNB film has an electron lifetime approximately one order of magnitude longer than the P25 nanoparticle film (Fig. 4b). This

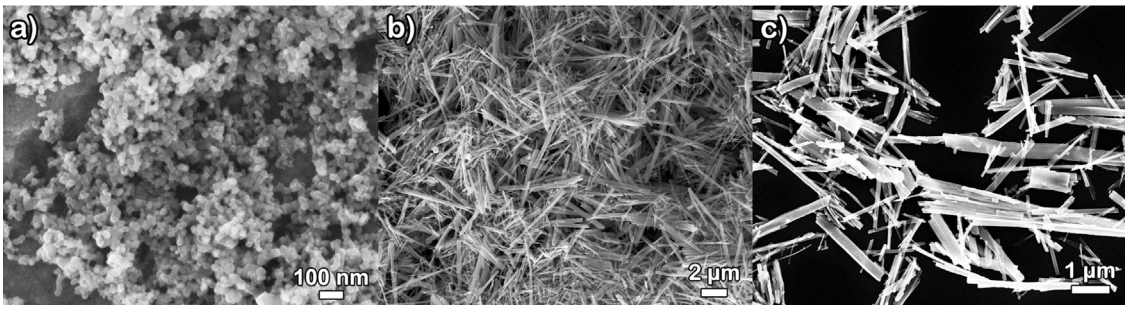

Fig. 2. FESEM images of (a) P25, (b) TNB, and (c) Ag-TNB.

suggests that TNB supresses the recombination pathways at the photoanode interface better than TiO_2 nanoparticles. Even though the electron lifetime is greater using nanobelts compared to nanoparticles, there is no statistical significant difference between the P25 and TNB in HTPA formation rate or MG removal rate (Table S2A). However, this may be attributed to the higher surface area in P25 ($57\ m^2\ g^{-1}$) compared to TNB ($20\ m^2\ g^{-1}$). TNB is also more prone to aggregation when dispersed in solution due to increased size in one dimension (μm range) compared to nanoparticles.

Generally, it is the case that the higher the surface area of the TiO_2 nanomaterial, the higher the apparent reaction rate. The zeta potential magnitude of nanobelts is lower than P25, which indicates that TNB will aggregate faster compared to P25 nanoparticles due to lower repulsion forces. The addition of Ag on TNB improved the electron-hole pair generation as shown by the increased HTPA formation rate and MG degradation rate via hole and hydroxyl radical in Fig. 3.

3.3. TPA degradation under varied duty cycles

To determine the effect of duty cycle on TiO_2 photocatalysis, the duty cycle was tested at 10%, 25%, 50%, 75%, and 100% at a constant pulse frequency (ν = 1 Hz). Absolute and normalized rates of HTPA under the various duty cycles were tabulated (Table S1) and post-hoc comparison tests were conducted (Table S2B). The normalized rate was given as:

$$Norm.\ \ k_1 = \frac{k_1}{0.01 \times \gamma(\%)} \tag{8}$$

The absolute and normalized rates of formation of HTPA (Fig. 5a) and the ratio of the normalized rate of HTPA formation at a specific duty cycle γ to the HTPA formation rate at continuous illumination (γ = 100%), $k_{1,DC}$:$k_{1,DC=100\%}$, were plotted for P25, TNB, and Ag-TNB (Fig. 5b). Under continuous illumination, Ag-TNB has an increased HTPA formation rate compared to P25 and TNB by a factor of 1.33 and 2.59, respectively.

The continuous introduction of photons results in a build-up of charges (e_{cb}^{-}/h_{vb}^{+}) that can favour undesirable recombination processes [53,54]. This effect can be shown through the reaction order of photocatalysis at various intensities. There is an initial linear dependency of the photocatalytic reaction rate on radiant flux (ϕ) that eventually changes into a square-root dependency ($\phi^{1/2}$) above a threshold radiant flux value. As the radiant flux increases, the concentrations of photo-electrons and holes increases, which exponentially increases the band-to-band recombination rate, r_R, defined as [18]:

$$r_R = k_R[e^-][h^+] = k_R[e^-]^2 \tag{9}$$

where k_R is the recombination rate coefficient, $[e^-]$ is the electron concentration, and $[h^+]$ is the hole concentration.

It was found that the lowest duty cycle tested (γ = 10%) had a significant increase in the normalized HTPA formation rate compared to continuous illumination for P25 and TNB experiments (P25: $p < 0.000$; TNB: $p < 0.000$). At γ = 10%, the normalized HTPA rate was 1.75, 1.40, and 0.70 times the HTPA formation rate at continuous illumination for P25, TNB, and Ag-TNB nanomaterials, respectively. In the case of P25 and, to a lesser extent, TNB, there was an improved normalized HTPA formation rate at low duty cycles (γ = 10%). This improvement is due to the introduction of a dark period that is beneficial in limiting the number of excess charges on the surface that tend to recombine [29,54].

In the case of Ag-TNB, the duty cycle confirms that the recombination losses are not of the same magnitude to P25 and TNB. Lowering the duty cycle was detrimental to the photonic efficiency for

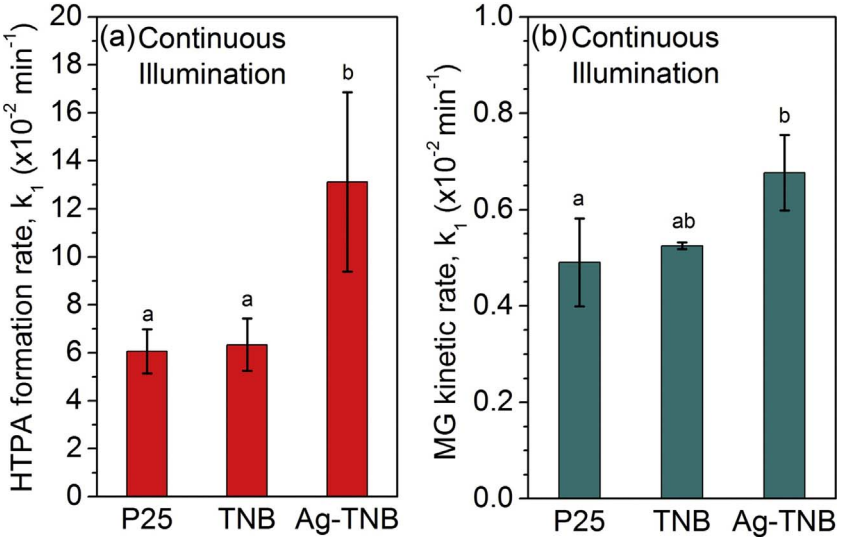

Fig. 3. (a) HTPA and (b) MG kinetic rates for P25, TNB, and Ag-TNB nanomaterials. Bars that do not share a common letter are significantly different at α = 0.05 significance level as determined by one-way ANOVA using the Holm-Sidak post-hoc test.

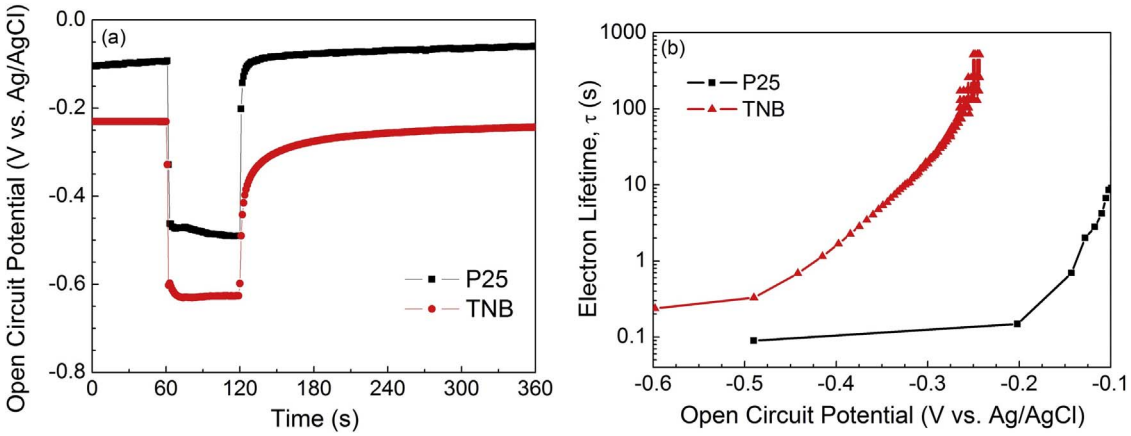

Fig. 4. (a) Open circuit potential and (b) electron life of P25 and TNB.

Ag-TNB (Fig. 5). Ag nanoparticles on TNB form a metal-semiconductor and the Ag serves as an "electron sink" that collect electrons, while holes are left on the TiO_2 surface. The enhanced charge separation at the metal-TiO_2 interface has been attributed to the formation of a Schottky energy barrier that prevents recombination in the depletion region [55]. Because of lower recombination, a dark period is not necessary compared to other nanomaterials. Therefore, higher light intensities can be used for Ag-TNB without photonic losses. The normalized HTPA formation rate was detrimental when lowering the duty cycle. This indicates that other processes may be occurring under continuous UV irradiation that increases the normalized reaction rate, such as localized surface plasmon resonance (LSPR) [34,56–58].

3.4. TPA degradation under varied frequency

The HTPA formation rate was measured under various pulse frequencies (ν = 25 Hz, 5 Hz, 0.5 Hz, and 0.05 Hz) at a constant duty cycle of γ = 50% for P25, TNB, and Ag-TNB in Fig. 6 (See Table S2C for one-way ANOVA test). As the frequency increases, the UV irradiation approaches continuous illumination [54,59]. There was a statistical difference using P25 at a pulse frequency of 0.05 Hz compared to all other frequencies tested (25 Hz: $p = 0.0006$; 5 Hz: $p = 0.0002$; 0.5 Hz: $p = 0.0018$, $\alpha = 0.05$). There was no statistical difference in HTPA formation for TNB when increasing the pulse frequency. Furthermore, there was a statistical difference in HTPA formation rate at a pulse frequency of 25 Hz compared to 0.05 Hz for Ag-TNB samples ($\alpha = 0.10$). Because high frequency CPI mimics continuous illumination, the results confirm the observations in the duty cycle experiments, in which Ag-TNB produced higher formation rates when UV light exposure was increased.

P25 experiments indicate an improvement in HTPA formation at higher frequencies tested compared to 0.05 Hz as shown in Fig. 6 (See Table S2 B for one-way ANOVA test), which may be due to two possible mechanisms: (i) the excess charge under longer illumination periods and (ii) fragmentation processes in TiO_2 particle networks that generate new adsorption sites from aggregates from illumination [54,60,61]. Under 0.05 Hz pulse frequency, HTPA formation kinetics for P25 reach steady-state due to the long UV exposure time of 10 s follow by a dark period of 10 s. This increased period permits excess charge build-up that increases recombination. Increasing the frequency from 0.05 Hz to a higher pulse frequency reduces the steady state time and increases the HTPA formation rate, which was found to occur in the study by Bahnemann et al. [62] Under aqueous conditions, TiO_2 nanoparticles can attract other nanoparticles and aggregate due to electrostatic and van der Waals interactions. The concept of photoinduced disaggregation was proposed by Bahnemann's group as explanation for higher oxidation using intermittent pulsing [60,63]. Their group attributed the increase in the quantum yield of formic acid oxidation under repetitive laser-pulses to disaggregation of nanoparticles and fragmentation of networks that promote additional adsorption sites for reactants. Irradiation of sufficient energy can partially disaggregate nanoparticles from their aggregates, increasing diffusion. This has been demonstrated through dynamic light scattering studies and membrane filtration comparisons under dark and light conditions in other studies, where the hydrodynamic diameter of TiO_2 aggregates can be reduced via light exposure [43,64]. Agglomerated TiO_2 particles not only increase in

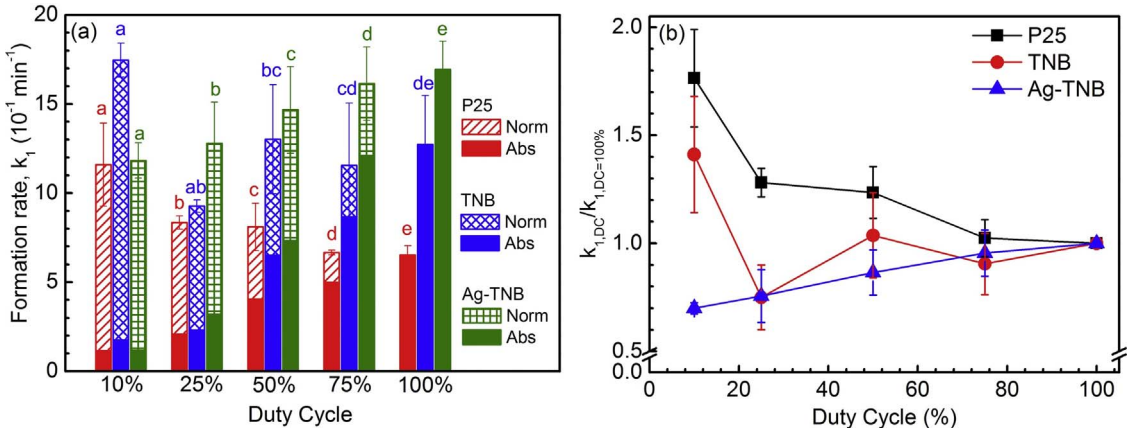

Fig. 5. (a) Absolute (filled) and normalized (patterned) formation rate of TPA, k_1, at various duty cycles using P25, TNB, and Ag-TNB nanomaterials; (b) $k_{1,DC}/k_{1,DC=100\%}$ ratio vs. duty cycle. Bars that do not share a common letter are significantly different at $\alpha = 0.05$ significance level as determined by one-way ANOVA using the Holm-Sidak post-hoc test to compare the formation rates at various duty cycles.

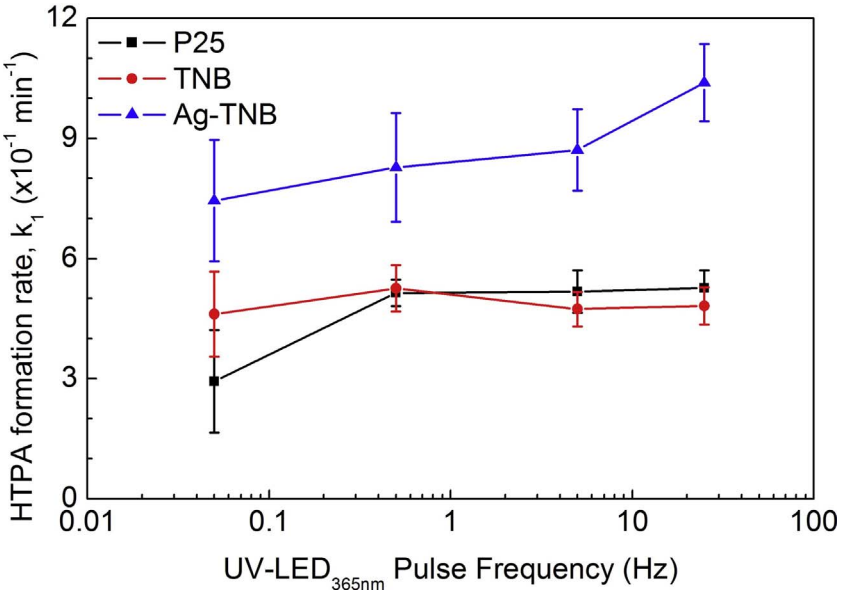

Fig. 6. HTPA formation rate as a function of frequency.

catalyst surface area upon disaggregation, but also acts as an antenna for transferring photon energy from the site of absorption to the site of reaction through a network effect [60].

Derjaguin, Landau, Vervey, and Overbeek (DLVO) theory was used to ascertain whether UV-LEDs have sufficient energy to dislodge nanoparticles from aggregates. Electrostatic repulsion forces and van der Waals attraction forces are taken into consideration in determining how these forces interact with particles. There exists a deep energy well, called the primary minimum, that traps particles that are below the energy well and coalesce. At larger separation distances, the energy profile passes through a shallow energy well, referred to as the secondary minimum [43]. The force-separation distance profile for TiO_2 nanoparticles was calculated (See Section S4 in the Supporting Information). The calculation indicates that 3.9×10^{-21} J (0.95 k_bT) are needed for a particle to escape the secondary minimum well. When irradiated with UV-LED, each particle can absorb up to 1.7×10^{-17} J s^{-1}. This energy from UV-LEDs is sufficient to dislodge a particle in the secondary minimum from agglomerates.

In the case of TNB experiments, there was no significant change in the HTPA formation rate when increasing the pulse frequency as indicated in Fig. 6 (See Table S2C for one-way ANOVA test). This may be due to TNB having lower surface area and greater dimensions compared to nanoparticles, which increases the energy required for a particle to dislodge from the secondary minimum. Anisometric particles, such as nanorods and nanowires, are also likely to aggregate under the secondary minimum [65]. The degree of aggregation is dependent on shape and is most favourable for platelets, less favourable for rods and cylinders, and the least favourable for spherical nanoparticles [65].

3.5. Implications of CPI in photocatalyst application

CPI has the benefit in reducing energy costs for TiO_2 photocatalysts and the evaluation of the treatment energy costs is one aspect that requires attention. Since the UV/TiO_2 process represents a significant amount of operating cost when it is scaled, figures-of-merit based on electrical energy consumption may be informative. In this case, electrical energy per order (E_{EO}), defined as the number of kilowatt hours of electrical energy required to degrade HTPA by one order of magnitude in a unit volume containing TPA as the starting compound. The E_{EO} (kWh m^{-3} order^{-1}) can be calculated [66,67]:

$$E_{EO} = \frac{38.4 P_{el}}{V \times k_2} \quad (11)$$

where P_{el} is the input power (kW) to the UV-LED system, V is the volume of water (L) in the reactor, k_2 is the degradation constant of HTPA (min^{-1}), and the constant multiplier accounts for conversions to kWh m^{-3} order^{-1}.

The addition of CPI can reduce the energy required to operate a batch reactor and under UV treatment options. The E_{EO} of HTPA degradation under UV-LED CPI-controlled TiO_2 photocatalysis (P25, TNB, and Ag-TNB) was determined under a favourable CPI condition (ν = 25 Hz, γ = 50%) and continuous illumination (Fig. 7). Ag-TNB under the CPI condition requires only 50% to 55% of the E_{EO} compared to P25 and TNB. Additionally, under the chosen CPI condition, Ag-TNB and P25 require 27% and 39% less E_{EO} than under continuous illumination. The use of TNB did not change under both light conditions. It may be beneficial to investigate catalysts under operational parameters such as CPI in terms of E_{EO} and compare other batch reactor setups with similar chemical compounds of interest [66,67] as kinetic rates alone do not take into account the reactor parameters.

4. Conclusions

TNB and Ag-TNB nanomaterials were synthesized using a hydrothermal synthesis method. The formation of P25 to TNB nanomaterials decreased the grain boundary defects that increase recombination

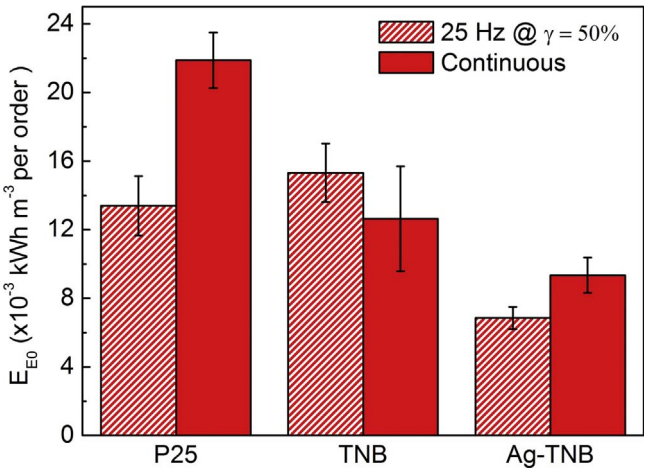

Fig. 7. Energy per order magnitude of UV-LED/TiO_2 process under CPI and continuous illumination.

reactions. Using open-circuit potential measurements, 1-D TiO_2 provides a greater charge-separation than P25 nanoparticles. P25 and TNB have a greater photonic efficiency at the lowest duty cycle (γ = 10%) tested due to excess charge build-up under continuous illumination which leads to recombination losses. Ag deposition onto TNB reduces the recombination and increases the HTPA formation rate due to the presence of metal-semiconductor junctions. The Ag-TNB experiments demonstrate detrimental performance when lowering the duty cycle, which may be due to the effective charge separation under a photon-limited regime and/or the LSPR effects that enhance reaction rates under illumination. P25 shows a slight increase in HTPA formation rate when the frequency is increased from 0.05 Hz, whereas TNB shows no change in formation rate when frequency is increased because of the shape in aggregation and increased energy required from UV-LEDs to dislodge TiO_2 particles from the secondary minimum of TNB. The energy per order of magnitude was the lowest for Ag-TNB under a high frequency CPI condition compared to the catalysts tested and continuous illumination.

Acknowledgments

This work has been financially supported by the Natural Sciences and Engineering Research Council of Canada (grant number: STPG-494554-2016) through a strategic project grant and the Schwartz-Reisman Foundation through the Waterloo Institute of Nanotechnology − Technion University grant. We would also like to thank Andrew Kacheff from Waterloo Structural Analysis Platform at the Waterloo Institute of Technology for BET surface area analysis.

Appendix A. Supplementary data

Supplementary data associated with this article can be found, in the online version, at http://dx.doi.org/10.1016/j.jece.2017.08.019.

References

[1] A. Fujishima, T.N. Rao, D.A. Tryk, Titanium dioxide photocatalysis, J. Photochem. Photobiol. C Photochem. Rev. 1 (2000) 1–21, http://dx.doi.org/10.1016/S1389-5567(00)00002-2.

[2] H. Dong, G. Zeng, L. Tang, C. Fan, C. Zhang, X. He, Y. He, An overview on limitations of TiO2-based particles for photocatalytic degradation of organic pollutants and the corresponding countermeasures, Water Res. 79 (2015) 128–146, http://dx.doi.org/10.1016/j.watres.2015.04.038.

[3] F.B. Li, X.Z. Li, The enhancement of photodegradation efficiency using Pt–TiO2 catalyst, Chemosphere 48 (2002) 1103–1111, http://dx.doi.org/10.1016/S0045-6535(02)00201-1.

[4] X.Z. Li, F.B. Li, Study of Au/Au3+-TiO2 Photocatalysts Toward Visible Photooxidation for Water and Wastewater Treatment, (2001), http://dx.doi.org/10.1021/ES001752W.

[5] R. Asahi, T. Morikawa, T. Ohwaki, K. Aoki, Y. Taga, Visible-light photocatalysis in nitrogen-doped titanium oxides, Science (80-.) 293 (2001).

[6] A. Zaleska, J.W. Sobczak, E. Grabowska, J. Hupka, Preparation and photocatalytic activity of boron-modified TiO2 under UV and visible light, Appl. Catal. B Environ. 78 (2008) 92–100, http://dx.doi.org/10.1016/j.apcatb.2007.09.005.

[7] N. Shi, X. Li, T. Fan, H. Zhou, J. Ding, D. Zhang, H. Zhu, Biogenic N-I-codoped TiO 2 photocatalyst derived from kelp for efficient dye degradation, Energy Environ. Sci. 4 (2011) 172–180, http://dx.doi.org/10.1039/C0EE00363H.

[8] W. Ho, J.C. Yu, S. Lee, Low-temperature hydrothermal synthesis of S-doped TiO2 with visible light photocatalytic activity, J. Solid State Chem. 179 (2006) 1171–1176, http://dx.doi.org/10.1016/j.jssc.2006.01.009.

[9] S.-L. Chen, A.-J. Wang, C.-T. Hu, C. Dai, J.B. Benziger, Enhanced photocatalytic performance of nanocrystalline TiO2 membrane by both slow photons and stop-band reflection of photonic crystals, AIChE J. 58 (2012) 568–572, http://dx.doi.org/10.1002/aic.12712.

[10] W. Wang, J. Zhang, F. Chen, D. He, M. Anpo, Preparation and photocatalytic properties of Fe3+-doped Ag@TiO2 core-shell nanoparticles, J. Colloid Interface Sci. 323 (2008) 182–186, http://dx.doi.org/10.1016/j.jcis.2008.03.043.

[11] W. Zhou, G. Du, P. Hu, G. Li, D. Wang, H. Liu, J. Wang, R.I. Boughton, D. Liu, H. Jiang, Nanoheterostructures on TiO2 nanobelts achieved by acid hydrothermal method with enhanced photocatalytic and gas sensitive performance, J. Mater. Chem. 21 (2011) 7937, http://dx.doi.org/10.1039/c1jm10588d.

[12] T. Hirakawa, P.V. Kamat, Charge separation and catalytic activity of Ag@TiO2 core-shell composite clusters under UV-irradiation, J. Am. Chem. Soc. 127 (2005) 3928–3934, http://dx.doi.org/10.1021/ja042925a.

[13] K. Awazu, M. Fujimaki, C. Rockstuhl, J. Tominaga, H. Murakami, Y. Ohki, N. Yoshida, T. Watanabe, A plasmonic photocatalyst consisting of silver nanoparticles embedded in titanium dioxide, J. Am. Chem. Soc. 130 (2008) 1676–1680, http://dx.doi.org/10.1021/ja076503n.

[14] J.-C. Xu, M. Lu, X.-Y. Guo, H.-L. Li, Zinc ions surface-doped titanium dioxide nanotubes and its photocatalysis activity for degradation of methyl orange in water, J. Mol. Catal. A Chem. 226 (2005) 123–127, http://dx.doi.org/10.1016/j.molcata.2004.09.051.

[15] Z. Jiang, F. Yang, N. Luo, B.T.T. Chu, D. Sun, H. Shi, T. Xiao, P.P. Edwards, Solvothermal synthesis of N-doped TiO2 nanotubes for visible-light-responsive photocatalysis, Chem. Commun. 0 (2008) 6372, http://dx.doi.org/10.1039/b815430a.

[16] Z. Xiong, X.S. Zhao, Nitrogen-doped titanate-anatase core-shell nanobelts with exposed {101} anatase facets and enhanced visible light photocatalytic activity, J. Am. Chem. Soc. 134 (2012) 5754–5757, http://dx.doi.org/10.1021/ja300730c.

[17] G. Ma, X. Zhao, J. Zhu, Microwave hydrothermal synthesis of rutile Tio_2 nanorods, Int. J. Mod. Phys. B 19 (2005) 2763–2768, http://dx.doi.org/10.1142/S0217979205031663.

[18] J.-M. Herrmann, Photocatalysis fundamentals revisited to avoid several misconceptions, Appl. Catal. B Environ. 99 (2010) 461–468, http://dx.doi.org/10.1016/j.apcatb.2010.05.012.

[19] C. Höfl, G. Sigl, O. Specht, I. Wurdack, D. Wabner, Oxidative degradation of aox and cod by different advanced oxidation processes: a comparative study with two samples of a pharmaceutical wastewater, Water Sci. Technol. 35 (1997) 257–264, http://dx.doi.org/10.1016/S0273-1223(97)00033-4.

[20] C. Martínez, M. Canle, L.M.I. Fernández, J.A. Santaballa, J. Faria, Aqueous degradation of diclofenac by heterogeneous photocatalysis using nanostructured materials, Appl. Catal. B Environ. 107 (2011) 110–118, http://dx.doi.org/10.1016/j.apcatb.2011.07.003.

[21] D.H. Quiñones, A. Rey, P.M. Álvarez, F.J. Beltrán, G. Li Puma, Boron doped TiO2 catalysts for photocatalytic ozonation of aqueous mixtures of common pesticides: diuron, o-phenylphenol, MCPA and terbuthylazine, Appl. Catal. B Environ. 178 (2015) 74–81, http://dx.doi.org/10.1016/j.apcatb.2014.10.036.

[22] W.H. Glaze, J. Kang, H. Douglas, Ozone: science & engineering: the journal of the international ozone association the chemistry of water treatment processes involving ozone, Hydrogen Peroxide and Ultraviolet Radiation (2008) 335–352.

[23] S. Irmak, O. Erbatur, A. Akgerman, Degradation of 17β-estradiol and bisphenol A in aqueous medium by using ozone and ozone/UV techniques, J. Hazard. Mater. 126 (2005) 54–62, http://dx.doi.org/10.1016/j.jhazmat.2005.05.045.

[24] M.R. Hoffmann, S.T. Martin, W. Choi, D.W. Bahnemannt, W.M. Keck, Environmental applications of semiconductor photocatalysis, Chem. Rev. 95 (1995) 69–96.

[25] J.M. Herrmann, Photocatalysis fundamentals revisited to avoid several misconceptions, Appl. Catal. B Environ. 99 (2010) 461–468, http://dx.doi.org/10.1016/j.apcatb.2010.05.012.

[26] I. Kim, H. Tanaka, Photodegradation characteristics of PPCPs in water with UV treatment, Environ. Int. 35 (2009) 793–802, http://dx.doi.org/10.1016/j.envint.2009.01.003.

[27] K. Tanaka, K. Abe, T. Hisanaga, Photocatalytic water treatment on immobilized TiO2 combined with ozonation, J. Photochem. Photobiol. A Chem. 101 (1996) 85–87, http://dx.doi.org/10.1016/S1010-6030(96)04393-6.

[28] K. Song, M. Mohseni, F. Taghipour, Application of ultraviolet light-emitting diodes (UV-LEDs) for water disinfection: a review, Water Res. 94 (2016) 341–349, http://dx.doi.org/10.1016/j.watres.2016.03.003.

[29] P. Xiong, J. Hu, Decomposition of acetaminophen (Ace) using TiO2/UVA/LED system, Catal. Today. 282 (2017) 48–56, http://dx.doi.org/10.1016/j.cattod.2016.03.015.

[30] S. Malato, J. Blanco, A. Vidal, P. Fernández, J. Cáceres, P. Trincado, J. Oliveira, M. Vincent, New large solar photocatalytic plant: set-up and preliminary results, Chemosphere 47 (2002) 235–240, http://dx.doi.org/10.1016/S0045-6535(01)00220-X.

[31] S. Malato, P. Fernández-Ibáñez, M.I. Maldonado, J. Blanco, W. Gernjak, Decontamination and disinfection of water by solar photocatalysis: recent overview and trends, Catal. Today 147 (2009) 1–59, http://dx.doi.org/10.1016/j.cattod.2009.06.018.

[32] V. Augugliaro, V. Loddo, M. Pagliaro, G. Palmisano, L. Palmisano, Clean by Light Irradiation, Royal Society of Chemistry, Cambridge, 2010, http://dx.doi.org/10.1039/9781849732031.

[33] K.J. Buechler, C.H. Nam, T.M. Zawistowski, Design and evaluation of a novel-Controlled periodic illumination reactor to study photocatalysis, Ind. Eng. Chem. Res. 38 (1999) 1258–1263, http://dx.doi.org/10.1021/ie9806139.

[34] E. Kowalska, R. Abe, B. Ohtani, Visible light-induced photocatalytic reaction of gold-modified titanium(iv) oxide particles: action spectrum analysis, Chem. Commun. 293 (2009) 241–243, http://dx.doi.org/10.1039/B815679D.

[35] S. Kim, S.J. Hwang, W. Choi, Visible light active platinum-ion-doped Ti photocatalyst, J. Phys. Chem. 126 (41) (2004) 13550–13559, http://dx.doi.org/10.1021/JP055278Y O2.

[36] R. Liang, A. Hu, J. Persic, Y. Norman Zhou, Palladium nanoparticles loaded on carbon modified TiO2 nanobelts for enhanced methanol electrooxidation, Nano-Micro Lett. 5 (2013) 202–212, http://dx.doi.org/10.5101/nml.v5i3.

[37] M.S. Lee, S.-S. Hong, M. Mohseni, Synthesis of photocatalytic nanosized TiO2–Ag particles with sol–gel method using reduction agent, J. Mol. Catal. A Chem. 242 (2005) 135–140, http://dx.doi.org/10.1016/j.molcata.2005.07.038.

[38] F. Zhang, Z. Cheng, L. Cui, T. Duan, A. Anan, C. Zhang, L. Kang, Controllable synthesis of Ag@TiO $_2$ heterostructures with enhanced photocatalytic activities under UV and visible excitation, RSC Adv. 6 (2016) 1844–1850, http://dx.doi.org/10.1039/C5RA17762F.

[39] X. Zhang, Y.L. Chen, R.S. Liu, D.P. Tsai, Plasmonic photocatalysis, Rep. Prog. Phys. 76 (2013) 46401, http://dx.doi.org/10.1088/0034-4885/76/4/046401 41 pages.
[40] R.B. Thurman, C.P. Gerba, G. Bitton, The molecular mechanisms of copper and silver ion disinfection of bacteria and viruses, Crit. Rev. Environ. Control. 18 (1989) 295–315, http://dx.doi.org/10.1080/10643388909388351.
[41] H. Eom, J.Y. Jung, Y. Shin, S. Kim, J.H. Choi, E. Lee, J.H. Jeong, I. Park, Strong localized surface plasmon resonance effects of Ag/TiO2 core–shell nanowire arrays in UV and visible light for photocatalytic activity, Nanoscale 6 (2014) 226–234, http://dx.doi.org/10.1039/C3NR04388F.
[42] R. Liang, A. Hu, W. Li, Y.N. Zhou, Enhanced degradation of persistent pharmaceuticals found in wastewater treatment effluents using TiO2 nanobelt photocatalysts, J. Nanoparticle Res. 15 (2013) 1990, http://dx.doi.org/10.1007/s11051-013-1990-x.
[43] S.W. Bennett, D. Zhou, R. Mielke, A.A. Keller, Photoinduced disaggregation of TiO2 nanoparticles enables transdermal penetration, PLoS One 7 (2012) e48719, http://dx.doi.org/10.1371/journal.pone.0048719.
[44] M.J. Arlos, R. Liang, M.M. Hatat-Fraile, L.M. Bragg, N.Y. Zhou, M.R. Servos, S.A. Andrews, Photocatalytic decomposition of selected estrogens and their estrogenic activity by UV-LED irradiated TiO2 immobilized on porous titanium sheets via thermal-chemical oxidation, J. Hazard. Mater. 318 (2016) 541–550, http://dx.doi.org/10.1016/j.jhazmat.2016.07.048.
[45] C.S. Turchi, D.F. Ollis, Photocatalytic degradation of organic water contaminants: mechanisms involving hydroxyl radical attack, J. Catal. 122 (1990) 178–192, http://dx.doi.org/10.1016/0021-9517(90)90269-P.
[46] U. Černigoj, M. Kete, U.L. Štangar, Development of a fluorescence-based method for evaluation of self-cleaning properties of photocatalytic layers, Catal. Today 151 (2010) 46–52, http://dx.doi.org/10.1016/j.cattod.2010.03.043.
[47] A. Hu, R. Liang, X. Zhang, S. Kurdi, D. Luong, H. Huang, P. Peng, E. Marzbanrad, K.D. Oakes, Y. Zhou, M.R. Servos, Enhanced photocatalytic degradation of dyes by TiO2 nanobelts with hierarchical structures, J. Photochem. Photobiol. A Chem. 256 (2013) 7–15, http://dx.doi.org/10.1016/j.jphotochem.2013.01.015.
[48] W.Q. Wu, H.S. Rao, Y.F. Xu, Y.F. Wang, C.Y. Su, D.B. Kuang, Hierarchical oriented anatase TiO2 nanostructure arrays on flexible substrate for efficient dye-sensitized solar cells, Sci. Rep. 3 (2013) 737–740, http://dx.doi.org/10.1038/srep01892.
[49] Z. Zheng, H. Liu, J. Ye, J. Zhao, E.R. Waclawik, H. Zhu, Structure and contribution to photocatalytic activity of the interfaces in nanofibers with mixed anatase and TiO2(B) phases, J. Mol. Catal. A Chem. 316 (2010) 75–82, http://dx.doi.org/10.1016/j.molcata.2009.10.002.
[50] A. Zaban, M. Greenshtein, J. Bisquert, Determination of the electron lifetime in nanocrystalline dye solar cells by open-circuit voltage decay measurements, ChemPhysChem 4 (2003) 859–864, http://dx.doi.org/10.1002/cphc.200200615.
[51] J.H. Bang, P.V. Kamat, Solar cells by design: photoelectrochemistry of TiO2 nanorod arrays decorated with CdSe, Adv. Funct. Mater. 20 (2010) 1970–1976, http://dx.doi.org/10.1002/adfm.200902234.
[52] J. Bisquert, A. Zaban, M. Greenshtein, I. Mora-Seró, Determination of rate constants for charge transfer and the distribution of semiconductor and electrolyte electronic energy levels in dye-Sensitized solar cells by open-Circuit photovoltage decay method, J. Am. Chem. Soc. 126 (2004) 13550–13559, http://dx.doi.org/10.1021/JA047311K.
[53] S.U. and, D.F. Ollis, Simple photocatalysis model for photoefficiency enhancement via controlled, Periodic Illumination (1997), http://dx.doi.org/10.1021/JP962649P.
[54] O. Tokode, R. Prabhu, L.A. Lawton, P.K.J. Robertson, Controlled periodic illumination in semiconductor photocatalysis, J. Photochem. Photobiol. A Chem. 319-320 (2016) 96–106, http://dx.doi.org/10.1016/j.jphotochem.2015.12.002.
[55] S. Litch, A.J. Bard, M. Stratmann, Encyclopedia of Electrochemistry, (2002), p. 6 (Weinheim, Germany).
[56] D.B. Ingram, S. Linic, Water splitting on composite plasmonic-Metal/Semiconductor photoelectrodes: evidence for selective plasmon-Induced formation of charge carriers near the semiconductor surface, J. Am. Chem. Soc. 133 (2011) 5202–5205, http://dx.doi.org/10.1021/ja200086g.
[57] I. Lee, J.Y. Park, K. Hong, J.H. Son, S. Kim, J.-L. Lee, et al., The effect of localized surface plasmon resonance on the emission color change in organic light emitting diodes, Nanoscale 8 (2016) 6463–6467, http://dx.doi.org/10.1039/C5NR07438J.
[58] R. Sellappan, M.G. Nielsen, F. González-Posada, P.C.K. Vesborg, I. Chorkendorff, D. Chakarov, Effects of plasmon excitation on photocatalytic activity of Ag/TiO2 and Au/TiO2 nanocomposites, J. Catal. 307 (2013) 214–221, http://dx.doi.org/10.1016/j.jcat.2013.07.024.
[59] J.G. Cornu Catherine, A.J. Colussi, M.R. Hoffmann, Quantum yields of the photocatalytic oxidation of formate in aqueous TiO2 suspensions under continuous and periodic illumination, J. Phys. Chem. B 105 (2001) 1351–1354, http://dx.doi.org/10.1021/JP003204A.
[60] C.Y. Wang, R. Pagel, J.K. Dohrmann, D.W. Bahnemann, Antenna mechanism and deaggregation concept: novel mechanistic principles for photocatalysis, Comptes Rendus Chim. 9 (2006) 761–773, http://dx.doi.org/10.1016/j.crci.2005.02.053.
[61] J.G. Sczechowski, C.A. Koval, R.D. Noble, A Taylor vortex reactor for heterogeneous photocatalysis, Chem. Eng. Sci. 50 (1995) 3163–3173, http://dx.doi.org/10.1016/0009-2509(95)00176-6.
[62] C.Y. Wang, R. Pagel, D.W. Bahnemann, J.K. Dohrmann, Quantum yield of formaldehyde formation in the presence of colloidal TiO 2-based photocatalysts: effect of intermittent illumination, platinization, and deoxygenation, J. Phys. Chem. B. 108 (2004) 14082–14092, http://dx.doi.org/10.1021/jp048046s.
[63] C.Y. Wang, R. Pagel, D.W. Bahnemann, J.K. Dohrmann, Quantum yield of formaldehyde formation in the presence of colloidal Ti-Based photocatalysts: effect of intermittent illumination, platinization, and deoxygenation, J. Phys. Chem. B. 108 (2004) 14082–14092, http://dx.doi.org/10.1021/JP048046S.
[64] D. Zhou, S.W. Bennett, A.A. Keller, Increased mobility of metal oxide nanoparticles due to photo and thermal induced disagglomeration, PLoS One 7 (2012) e37363, http://dx.doi.org/10.1371/journal.pone.0037363.
[65] E.M. Hotze, T. Phenrat, G.V. Lowry, Nanoparticle aggregation: challenges to understanding transport and reactivity in the environment, J. Environ. Qual. 39 (2010) 1910–1924 http://www.ncbi.nlm.nih.gov/pubmed/21284288.
[66] M.A. Behnajady, B. Vahid, N. Modirshahla, M. Shokri, Evaluation of electrical energy per order (E EO) with kinetic modeling on the removal of Malachite Green by US/UV/H 2 O 2 process, Desalination 249 (2009) 99–103, http://dx.doi.org/10.1016/j.desal.2008.07.025.
[67] Y. Ku, S.J. Shiu, H.C. Wu, Decomposition of dimethyl phthalate in aqueous solution by UV–LED/TiO2 process under periodic illumination, J. Photochem. Photobiol. A Chem. 332 (2017) 299–305, http://dx.doi.org/10.1016/j.jphotochem.2016.09.011.